

Article

Bifunctional g-C₃N₄/WO₃ Thin Films for Photocatalytic Water Purification

Maria Antoniadou, Michalis K. Arfanis, Islam Ibrahim and Polycarpus Falaras *

Institute of Nanoscience and Nanotechnology, National Center for Scientific Research “Demokritos”,
15341 Agia Paraskevi, Athens, Greece; m.antoniadou@inn.demokritos.gr (M.A.);
m.arfanis@inn.demokritos.gr (M.K.A.); i.ibrahim@inn.demokritos.gr (I.I.)

* Correspondence: p.falaras@inn.demokritos.gr

Received: 30 October 2019; Accepted: 19 November 2019; Published: 21 November 2019



Abstract: A bifunctional thin film photocatalyst consisting of graphitic carbon nitride on tungsten trioxide (g-C₃N₄/WO₃) is introduced for the improvement of photocatalytic activity concerning hexavalent chromium reduction and methylene blue dye removal in water, compared to the bare, widely used WO₃ semiconductor. A bilayered structure was formed, which is important for the enhancement of the charge carriers' separation. The characterization of morphological, structural, optoelectronic, and vibrational properties of the photocatalysts permitted a better understanding of their photocatalytic activity for both dye degradation and Cr⁺⁶ elimination in water and the analysis of the photocatalytic kinetics permitted the determination of the corresponding pseudo-first-order reaction constants (*k*). Trapping experiments performed under UV illumination revealed that the main active species for the photocatalytic reduction of Cr⁺⁶ ions are electrons, whereas in the case of methylene blue azo-dye (MB) oxidation, the activation of the corresponding photocatalytic degradation comes via both holes and superoxide radicals.

Keywords: tungsten oxide; graphitic carbon nitride; photocatalysis; methylene blue; hexavalent chromium

1. Introduction

Photocatalytic materials based on oxide semiconductors are attractive candidates for environmental applications, such as pollutants degradation and water purification [1]. The semiconductor's solar light-driven activity is originated from the electrons (e⁻) excitation to the conduction band, leaving positively-charged holes (h⁺) in the valence band. The photogenerated charge carriers are able to react with water molecules, hydroxyl anions, and molecular oxygen to generate hydroxyl (•OH) and superoxide anion (O₂^{•-}) radicals. These reactive oxygen species can attack organic and inorganic contaminants, which could be degraded or transformed following oxidation and/or reduction reactions. Titanium dioxide is among the most studied semiconducting materials but its practical use is limited to the UV range, due to the high energy gap (3.0–3.2 eV). Recent literature works also focus on tungsten trioxide (WO₃), which presents very interesting optoelectronic properties, justifying a broader application field, including electrochromic systems, energy conversion devices, and gas sensors [2]. WO₃ has an ideal band gap 2.4–2.8 eV [3,4], shows high chemical stability, and is a non-toxic semiconductor. However, the photocatalytic degradation of organic pollutants is not very efficient as the conduction band lies in a low unfavorable position, where the recombination of the photogenerated electrons with holes cannot be avoided [5]. On the other hand, since 2009, when Wang et al. [6] reported the synthesis of graphitic carbon nitride (g-C₃N₄) photocatalyst, significant efforts have been made to introduce this metal-free semiconductor in photocatalytic pollutants degradation and hydrogen production. The g-C₃N₄ band gap is about 2.7 eV and its conduction band is at about

1.12 eV, thus the photogenerated electrons have high reductive ability. Furthermore, the material can be easily prepared and its fabrication cost mainly comprises that of a simple heat treatment of melamine precursor in ambient pressure. Nevertheless, the bare $g\text{-C}_3\text{N}_4$ presents high recombination rate of the photoinduced carriers (electron-hole pairs), which affects the photocatalytic activity. To enhance the separation of photogenerated charges and improve the efficiency of the photocatalytic process, heterojunction composites or multilayered structures have been introduced, including doping and coupling $g\text{-C}_3\text{N}_4$ with metal, nonmetal and other semiconductor materials, such as $\text{Ag}/g\text{-C}_3\text{N}_4$ [7], $\text{CdS}/g\text{-C}_3\text{N}_4$ [8], $\text{ZnO}/g\text{-C}_3\text{N}_4$ [9], $\text{AuPd}/g\text{-C}_3\text{N}_4$ [10], and $\text{WO}_3/g\text{-C}_3\text{N}_4$ [11]. In the last case, the composite heterostructure presents a much higher photocatalytic activity than the pristine $g\text{-C}_3\text{N}_4$ and WO_3 components [12–14].

Moreover, recent investigations in the field of photocatalysis attempt to explore novel trends and present perspectives of innovative nanostructured photocatalysts inside and outside the well-established frame of advanced oxidation processes (AOPs). Special focus is paid on expanding the field borders by including advanced reduction processes (ARPs) and relating technological applications (ARTs) [15]. In this direction, here we report for the first time the development of bifunctional composite $g\text{-C}_3\text{N}_4/\text{WO}_3$ thin film photocatalysts and their action in both oxidation and reduction reactions. We put particular emphasis on characteristic pollutants resulting from intensive industrial activity mainly in textiles dying (production of colored fabrics, yarns, and fibers) and metal finishing/plating applications, by examining the degradation of methylene blue azo-dye and the elimination of inorganic hexavalent chromium model pollutant compounds in water.

2. Materials and Methods

All chemicals with analytical grade were used without further purification. Unless otherwise indicated, reagents were obtained from Sigma-Aldrich and were used as received. Melamine and tungsten powder were purchased from Acros and Alfa Aesar, respectively. Methylene blue was purchased from Fluka and hexavalent chromium ions from Riedel de Haen. Potassium bromate (KBrO_3), potassium iodide (KI), benzoquinone (BQ), and isopropyl alcohol (IPA) were purchased from Acros-Organics. Deionized water was used throughout. Microscope slides were purchased from Fisher Scientific.

2.1. Synthesis of WO_3 Precursor Solution

Tungsten powder (0.5 g) was reacted with aqueous hydrogen peroxide (H_2O_2 , 15 mL, 30%) under sonication for 4 h until a transparent solution was obtained. The excess of H_2O_2 was catalytically decomposed by immersing a Pt foil into the solution for 12 h. Then, 3 mL of absolute ethanol and 0.3 g of Triton X-100 surfactant were added to the solution [16].

2.2. Preparation of $g\text{-C}_3\text{N}_4$

Bulk $g\text{-C}_3\text{N}_4$ was prepared by calcination of melamine 10 g in a crucible at 550 °C for 4 h with a ramp rate 5 °C/min. The resulting yellow agglomerates were ground into powder in an agate mortar and collected. The powder passed a second annealing process at 500 °C for 2 h with a ramp rate 5 °C/min and after cooling to room temperature its color became light yellow. To prepare a uniform suspension, 5 mg of the powder were added to a solution containing 25 μL Nafion perfluorinated solution, 145 μL of absolute ethanol and 84 μL of deionized water followed by sonication for 4 h.

2.3. Preparation of Bilayered $g\text{-C}_3\text{N}_4/\text{WO}_3$ Thin Films

The photocatalyst films were prepared as follows. Microscope glass slides (2 cm \times 2 cm) were cleaned with a detergent followed by sonication in ethanol, acetone, and isopropyl alcohol. Then, a quantity of 80 μL WO_3 sol-gel was casted on the glass followed by annealing at 500 °C. The high annealing temperature was required to assure that any organic content was removed. The procedure repeated once more before casting the $g\text{-C}_3\text{N}_4$ suspension and the films were again calcined at 450 °C.

2.4. Characterization Techniques

The films morphology was examined with a PHILIPS Quanta FEI Inspect SEM microscope, with a tungsten filament operating at 25 KeV. To evaluate the samples crystallinity, XRD and Raman measurements were conducted. X-ray diffraction was performed using a Siemens D-diffractometer with Cu – $K_{\alpha 1}$ ($\lambda = 1.5406 \text{ \AA}$) and Cu – $K_{\alpha 2}$ ($\lambda = 1.5444 \text{ \AA}$) radiation. For vibrational spectroscopy, a Renishaw InVia Reflex microscope, coupled with a Leica DMLC microscope, with 5 \times and 50 \times objectives lenses, and a laser source (emitting at 514.4 or 785 nm), was used. The absorption properties of the synthesized films were verified under UV/vis spectroscopy, using a UV/vis Hitachi 3010 spectrophotometer, equipped with an integrating sphere and BaSO₄ as reference.

2.5. Evaluation of the Photocatalytic Activity

The photocatalytic properties of WO₃ based films were examined under the degradation of the common organic azo-dye test pollutant methylene blue (MB, 3 μM), and the reduction of the inorganic hexavalent chromium ions (Cr⁺⁶/K₂Cr₂O₇, 98%, $0.48 \times 10^{-4} \text{ M}$) to trivalent. All experiments were performed in a photocatalytic reactor under UV-A illumination (four Sylvania UVA lamps 15 W/BLB, 350–390 nm, 0.5 mW cm^{-1}) for 2 h [17]. First, the films were immersed in 10 mL of the pollutant solutions and they were kept in dark for 1 h prior to illumination to achieve adsorption–desorption equilibrium. During the UV-A illumination, the characteristic absorption peak of MB at 664 nm was monitored with the photo-spectrophotometer every 30 min to determine the MB concentration. In the case of Cr⁺⁶, a colorimetric method was applied to monitor the reduction kinetics [18]. In particular, the Cr⁺⁶ complex with diphenylcarbazide (DPC, Merck 98%) metal ion indicator presented a characteristic absorption peak at 542 nm, proportional to its concentration. To detect the active species responsible for the photocatalytic mechanisms under UV illumination, trapping experiments were performed using different kinds of scavengers including KI (h⁺ quencher), IPA ($\bullet\text{OH}$ quencher), BQ (O₂^{•-} quencher), and KBrO₃ (e⁻ quencher) [19].

3. Results and Discussion

3.1. Characterization

The SEM micrographs of tungsten trioxide revealed that these films present a rough but homogeneous surface. At higher resolution, it is clear that elongated nanosized WO₃ distorted flakes were formed across the glass substrate, with width of around 70 nm and length varying from 0.8 to 1.7 μm (Figure 1a). Upon the addition of g-C₃N₄, well dispersed carbonic clouds of different sizes were detected on the WO₃ surface, without affecting the oxide morphology underneath. These nebulous structures consist of randomly oriented carbon nitride agglomerates (Figure 1b). The cross-section image of the composite film (Figure 1c), revealed a thick and uniform WO₃ layer at the bottom, with thickness close to 4.5 μm , while the upper layer of g-C₃N₄ is limited to 1.1 μm .

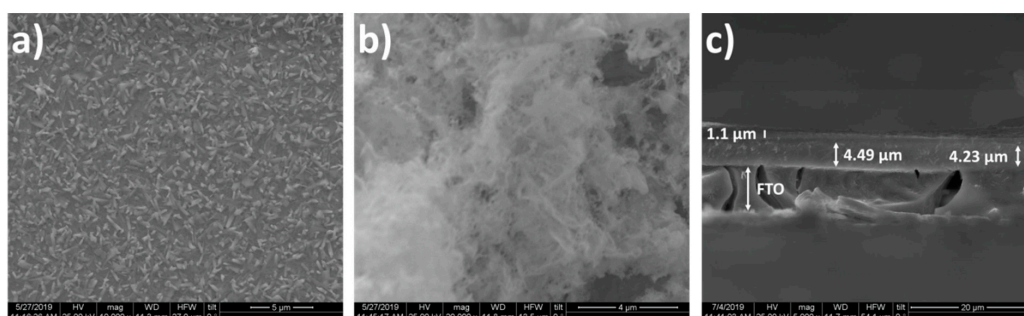


Figure 1. SEM top images of WO₃ (a) and g-C₃N₄/WO₃ (b) films on fluorine-doped tin oxide (FTO) substrates at 5000 \times magnification. The respective cross-section image (c) is also shown.

The XRD patterns in Figure 2 show that the WO_3 crystal is mainly crystallized in the cubic phase (JPDs Card No. 41.0905, marked as #), while the carbon nitride deposition did not cause any phase transformation of the oxide. It is remarkable that the main diffraction peaks of WO_3 at 25.9° , 33.7° , 48.9° , and 55.9° correspond to (100), (110), (200), and (210) crystal planes, respectively, which is in accordance with the formed nanoflake structure and confirms this preferred two-dimensional crystal orientation.

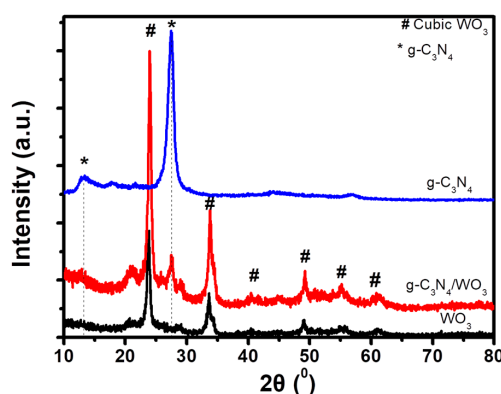


Figure 2. XRD patterns of WO_3 film (black), $g\text{-C}_3\text{N}_4/\text{WO}_3$ (red), and $g\text{-C}_3\text{N}_4$ (blue).

In addition, WO_3 impurities of different stoichiometry (e.g., $\text{WO}_{2.92}$, JPDs Card No. 30.1387) or different crystal symmetry cannot be excluded. Concerning the carbon nitride, the peaks located at 27.5° and 13.0° (JCPDS 87–1526, marked with * in Figure 2) are typical diffractions of amorphous graphitic nitride and they are ascribed as the in-plane structural packing and the interlayer stacking of the network, respectively [20,21]. It is noted that the low intensities of the carbon nitride in the bilayered film are possibly due to the good dispersion of $g\text{-C}_3\text{N}_4$ onto the WO_3 surface and its low crystallinity compared to the tungsten trioxide.

The investigation of WO_3 film with Raman spectroscopy is presented in Figure 3a. The Raman bands at around 807 and 708 cm^{-1} correspond to O–W–O symmetric and anti-symmetric stretching vibrations, respectively; the 272 and 327 cm^{-1} to bending vibrations of W–O–W; and the peak at the lower wavenumber of 139 cm^{-1} is due to lattice modes [22,23]. Nevertheless, it is clear that hydrated WO_3 ($\text{WO}_3 \cdot x\text{H}_2\text{O}$ formations, $x = 1, 2$ or $1/3$) coexist on the surface, as a shoulder is displayed at $740\text{--}780\text{ cm}^{-1}$ and two extra bands are located at 916 and 948 cm^{-1} , where the latter is assigned as W = O stretching mode [24,25]. Moreover, a wide shoulder in the range of $550\text{--}690\text{ cm}^{-1}$ may arise from traces of other crystallographic phases, which act as lattice distortions [26,27].

In the case of the $g\text{-C}_3\text{N}_4/\text{WO}_3$ composite films, there were spectral variations, related with the focusing area, as the optical microscope resolution allowed discriminating the deeper layer of the oxide (black areas on the inset of Figure 3b) and the carbonic layer on the top (yellow areas in the inset). When the microscope was focused on the oxide, the spectra were almost identical to the bare WO_3 film (Figure 3b). As expected, no bands of the carbon nitride were observed above 1000 cm^{-1} in this area [28]. Nevertheless, the characteristic G and D bands of carbonic materials did not appear during the study of $g\text{-C}_3\text{N}_4$ area, implying the material's high fluorescence under the 514.4 laser. It is also noted that the $g\text{-C}_3\text{N}_4$ layer blocked most of the WO_3 vibrations bands, permitting only specific bands to be detected. Interestingly, when replacing the excitation source by the NIR laser, the new $g\text{-C}_3\text{N}_4$ spectrum was much more detailed (Figure 3c). First, the G and D bands were recorded at 1350 and 1557 cm^{-1} , confirming the carbonic nature of the material [21]. The vibrations at 687 , 708 , 753 , and 990 cm^{-1} are clearly distinguished as modes of carbon nitride [29,30]. Moreover, the vibrational modes at 1113 and 1457 cm^{-1} were associated with the C–C and C=C stretching vibrations, while the mode at 1233 cm^{-1} is assigned as C=C bending mode [20]. The rest of the peaks were related to crystallites of s-triazine, melem, and melon units, as an expected sequence of carbon nitride synthesis by the combustion of melamine [21,29–31].

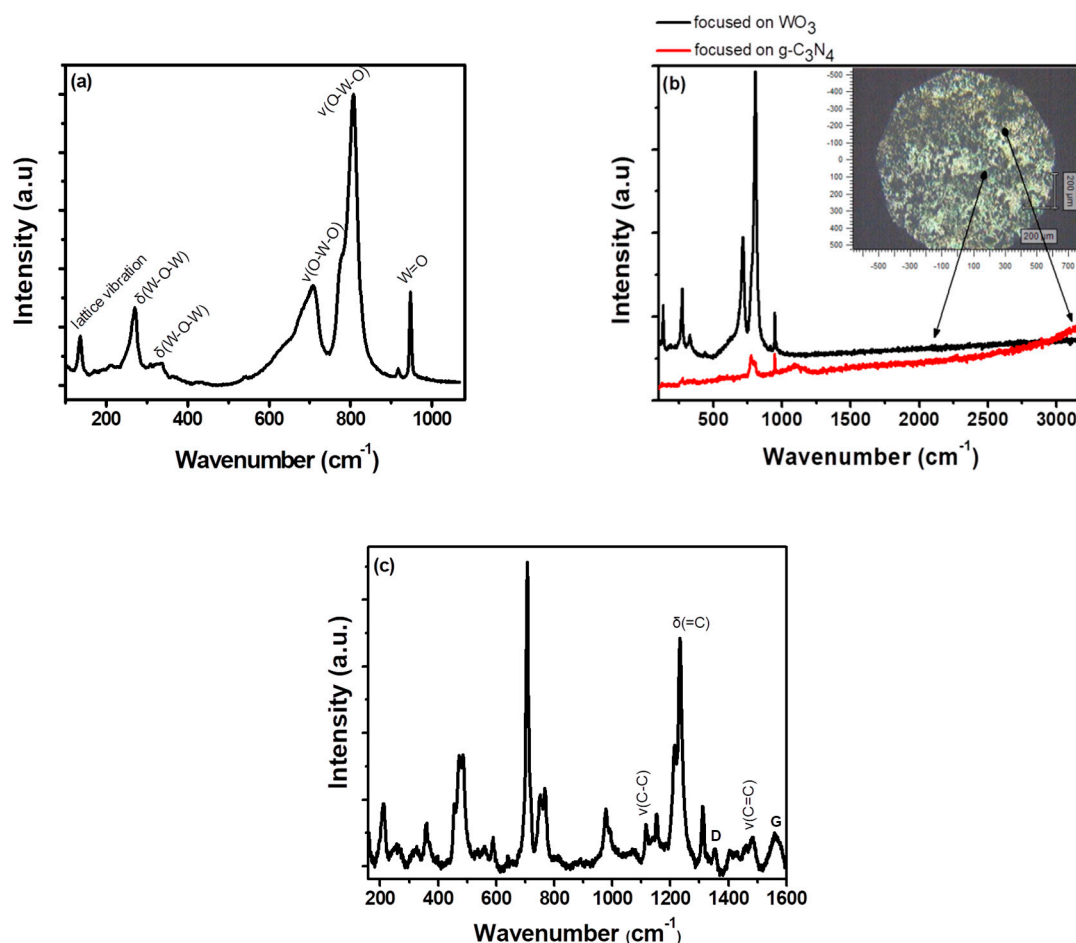


Figure 3. Raman spectra of WO_3 (a) and $\text{g-C}_3\text{N}_4/\text{WO}_3$ (b) films with the 514.4 laser, when focusing in the carbonic layer; and $\text{g-C}_3\text{N}_4/\text{WO}_3$ film with the NIR laser (c). The inset in (b) shows the measured areas for the mixed film: black for the WO_3 and yellow for the $\text{g-C}_3\text{N}_4$.

In addition, diffuse reflectance spectra in Figure 4, expressed in Kubelka-Munk units ($F(R)$), showed typical absorption properties of WO_3 materials. Their absorption surpassed UV part of solar light, reaching 450 nm, corresponding in energy gap of 2.71 eV in the Tauc plots (Figure 4b). The incorporation of $\text{g-C}_3\text{N}_4$ on top of WO_3 has not significantly changed the energy bad gap, as both materials have very similar energy gap values.

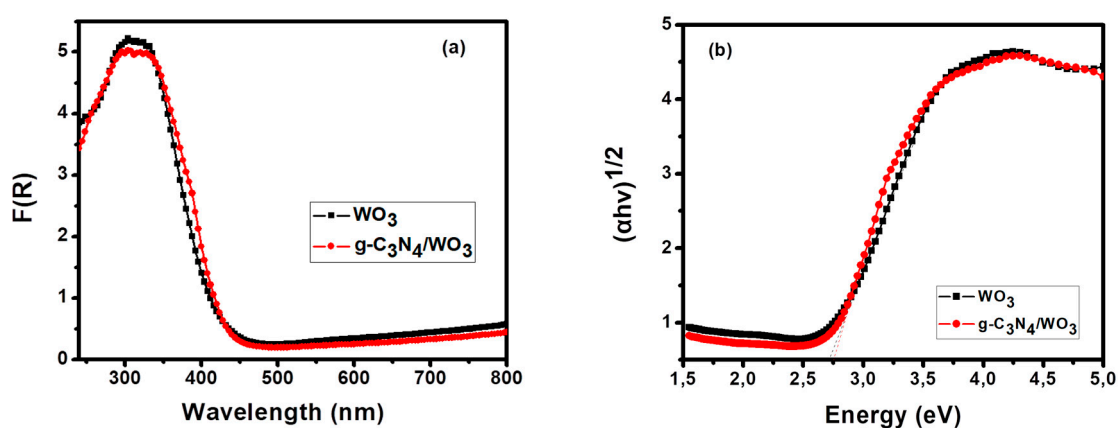


Figure 4. Absorption of WO_3 and $\text{g-C}_3\text{N}_4/\text{WO}_3$ films, expressed in $F(R)$ units (a); and the Tauc plots of films for the energy gap calculations (b).

3.2. Photocatalysis and Trapping Experiments

To evaluate the photocatalytic properties of WO_3 and $\text{g-C}_3\text{N}_4/\text{WO}_3$ materials, MB and Cr^{+6} were used as target pollutants. The chosen pollutants allow examining the catalyst in oxidation and reduction reactions pathways independently, expanding the possibility to use them in a wide range of applications.

3.2.1. Photocatalytic Oxidation of Methylene Blue

It is well known that methylene blue (MB) is a cationic dye pollutant, so intense adsorption was expected in the negative charged surface of WO_3 materials for the inert pH environment (pH \sim 7) [32]. For this reason, the MB concentration after the adsorption–desorption equilibrium was denoted as the solution's initial concentration.

As shown in Figure 5a, the $\text{g-C}_3\text{N}_4/\text{WO}_3$ films presented improved photocatalytic activity compared to the bare WO_3 films. In particular, after 2 h under UV-A illumination, almost 70% of MB was degraded when the bilayered $\text{g-C}_3\text{N}_4/\text{WO}_3$ film was used, while, with the use of WO_3 , it was limited to 65%. Likewise, the pseudo-first-order reaction constants (k) for MB oxidation were evaluated using the corresponding $\ln(C_0/C_t)$ against time plots (not shown), giving the values of 0.00299 and 0.00387 min^{-1} for WO_3 and $\text{g-C}_3\text{N}_4/\text{WO}_3$, respectively. Moreover, the $\text{g-C}_3\text{N}_4/\text{WO}_3$ films caused the N-demethylation of MB, since the main absorption peak of MB at 664 nm (Figure 5b) blue-shifted, indicating the formation of byproducts, such as Azure A, Azure B, Azure C, and Thionine [33]. In contrast, such a mechanism was not observed for WO_3 bare film.

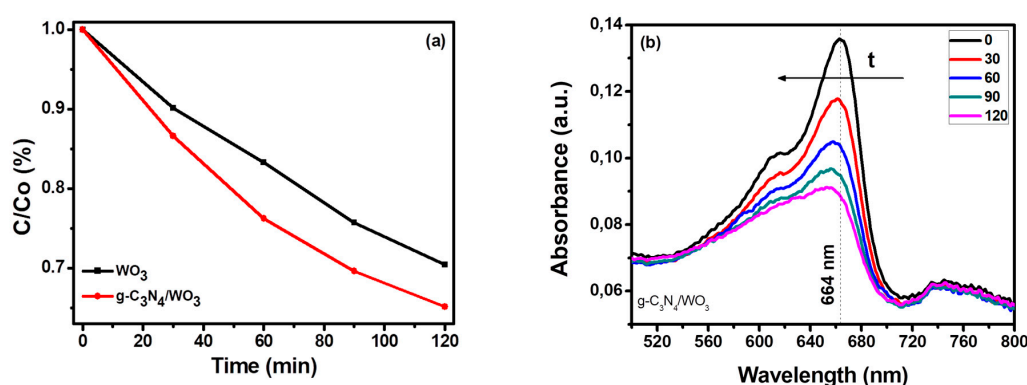


Figure 5. Photocatalytic removal of MB azo-dye by WO_3 (black line) and $\text{g-C}_3\text{N}_4/\text{WO}_3$ (red line) under UV-A illumination (a); and the blue-shift of the main peak of the MB at 664 nm, due to the N-demethylation (b).

3.2.2. Photocatalytic Reduction of Cr^{+6}

The photocatalytic reduction ability of the prepared catalysts was also evaluated using UV light, by immersing each film (WO_3 and $\text{g-C}_3\text{N}_4/\text{WO}_3$) in 15 mL of Cr^{+6} (5 mg from $\text{K}_2\text{Cr}_2\text{O}_7$ in 1 L DI H_2O) and adding six drops of M H_2SO_4 (0.2 mol/L). The solution was stirred in the dark (1 h) to obtain the equilibrium. Then, UV illumination was performed by using a white box photoreactor (50 cm \times 50 cm \times 30 cm) with four UV-A, 4-Sylvania TLD 15 W/08 lamps (350–390 nm, 0.5 mW/cm^2). The advancement of reaction was checked using UV-Visible spectroscopy ($\lambda_{\text{max}} = 542 \text{ nm}$).

The photocatalytic reduction of Cr^{+6} for the prepared films was evaluated under UV illumination, as presented in Figure 6. The percentage for Cr^{+6} reduction was 6.17% and 92.87% at 120 min for WO_3 and $\text{g-C}_3\text{N}_4/\text{WO}_3$, respectively. Furthermore, WO_3 film shows lower photocatalytic efficiency, comparing with bilayered film. The higher photocatalytic efficiency of the films might be attributed to facilitation of the electron–hole separation process [19,34]. In addition, the pseudo-first-order reaction constants (k) for Cr^{+6} reduction (to Cr^{+3}) were determined as 0.0007 and 0.017 min^{-1} for WO_3 and

g-C₃N₄/WO₃, respectively, further revealing the beneficial role of the graphitic carbon nitride top layer for enhancing the photocatalytic reduction activity of the bilayered films.

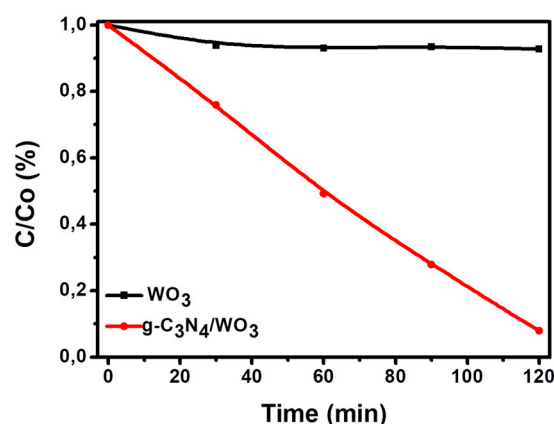


Figure 6. Photocatalytic reduction of Cr⁺⁶ to Cr⁺³ by WO₃ (black line) and g-C₃N₄/WO₃ (red line) under UV-A illumination.

To study the mechanism of the Cr⁺⁶ reduction and MB oxidation using the binary composite, and to detect the species that are responsible for redox reaction for both pollutants, trapping experiments were performed, under UV illumination, as presented in Figure 7a,b, respectively.

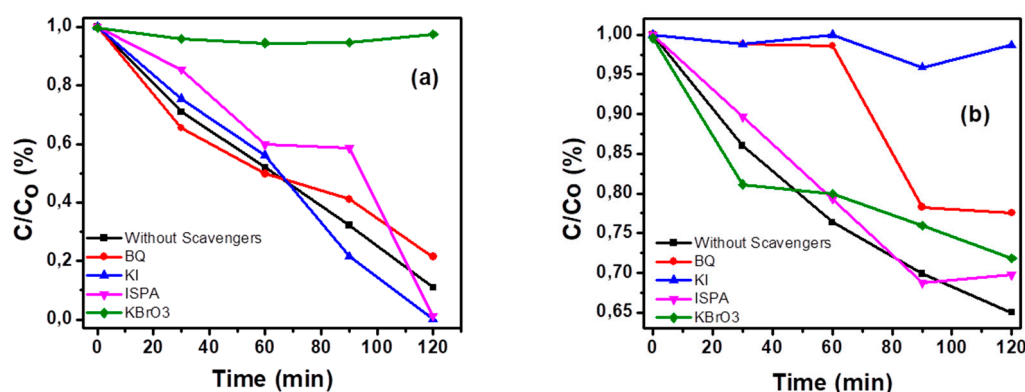


Figure 7. Scavengers effect on Cr⁺⁶ photocatalytic reduction (a); and MB photodegradation using the g-C₃N₄/WO₃ photocatalyst under UV irradiation (b).

When adding IPA (\bullet OH scavenger), BQ ($O_2^{\bullet-}$ scavenger), and KI (h^+ scavenger) no change was noticed for the reduction process. In contrast, KBrO₃ (e^- scavenger) addition led to blocking of photocatalytic reduction. Thus, electrons are the main active species in the photocatalytic reduction process. For MB oxidation, the addition of KBrO₃ and IPA did not affect the oxidation process, but addition of KI (h^+ scavenger) inhibited the oxidation process, and there was a decrease in photocatalytic oxidation process when adding BQ ($O_2^{\bullet-}$ scavengers), thus both holes and superoxide radicals are the main active species for the oxidation process [34–36].

4. Conclusions

Novel bifunctional photocatalytic films were prepared by consecutively depositing WO₃ and g-C₃N₄ materials. The composite films present elongated nanosized WO₃ distorted flakes onto which well dispersed g-C₃N₄ carbonic agglomerates were formed. These films present improved photocatalytic discoloration of MB and enhanced photocatalytic Cr⁺⁶ reduction activity, compared to pristine WO₃ photocatalyst, implying the successful interplay of the two catalysts, in agreement

with the characteristic structural, optoelectronic, and vibrational properties. The experiments using appropriate scavengers revealed that the main active species are electrons for reduction reactions and both holes and superoxide radicals for oxidation reactions.

Author Contributions: Conceptualization, M.A. and P.F.; methodology, M.A., M.K.A., I.I. and P.F.; investigation, M.A., M.K.A. and I.I.; writing—original draft preparation, M.A., M.K.A. and I.I.; writing—review and editing, P.F.; supervision, P.F.

Funding: This research was funded by: the Hellenic Foundation for Research and Innovation (HFRI) and the General Secretariat for Research and Technology (GSRT), under grant agreement No [2490]; the European Commission, Environment, LIFE17 ENV/GR/000387-PureAgroH₂O Programme; Prince Sultan Bin Abdulaziz International Prize for Water—Alternative Water Resources Prize 2014.

Acknowledgments: M. Antoniadou acknowledges support from the Hellenic Foundation for Research and Innovation (HFRI) and the General Secretariat for Research and Technology (GSRT), under grant agreement No [2490]. M. Arfanis and P. Falaras acknowledge support from the European Commission, Environment, LIFE17 ENV/GR/000387-PureAgroH₂O Programme. P. Falaras acknowledges support from Prince Sultan Bin Abdulaziz International Prize for Water—Alternative Water Resources Prize 2014.

Conflicts of Interest: The authors declare no conflict of interest.

References

1. Ibrahim, I.; Ali, I.O.; Salama, T.M.; Bahgat, A.A.; Mohamed, M.M. Synthesis of magnetically recyclable spinel ferrite (MFe₂O₄, M = Zn, Co, Mn) nanocrystals engineered by sol gel-hydrothermal technology: High catalytic performances for nitroarenes reduction. *Appl. Catal. B Environ.* **2016**, *181*, 389–402. [[CrossRef](#)]
2. Yan, M.; Wu, Y.; Zhu, F.; Hua, Y.; Shi, W. The fabrication of a novel Ag₃VO₄/WO₃ heterojunction with enhanced visible light efficiency in the photocatalytic degradation of TC. *Phys. Chem. Chem. Phys.* **2016**, *18*, 3308–3315. [[CrossRef](#)] [[PubMed](#)]
3. Su, X.T.; Xiao, F.; Li, Y.N.; Jian, Q.J.K.; Sun, J.; Wang, J.D. Synthesis of uniform WO₃ square nanoplates via an organic acid-assisted hydrothermal process. *Mater. Lett.* **2010**, *64*, 1232–1234. [[CrossRef](#)]
4. Wen, Z.H.; Wu, W.; Liu, Z.; Zhang, H.; Li, J.H.; Chen, J.H. Ultrahigh-efficiency photocatalysts based on mesoporous Pt–WO₃ nano hybrids. *Phys. Chem. Chem. Phys.* **2013**, *15*, 6773–6778. [[CrossRef](#)]
5. Karimi-Nazarabad, M.; Goharshadi, E.K. Highly efficient photocatalytic and photoelectrocatalytic activity of solar light driven WO₃/g-C₃N₄ nanocomposite. *Sol. Energy Mater. Sol. Cells* **2017**, *160*, 484–493. [[CrossRef](#)]
6. Wang, X.C.; Maeda, K.; Thomas, A.; Takanabe, K.; Xin, G.; Carlsson, J.M.; Domen, K.; Antonietti, M. A metal-free polymeric photocatalyst for hydrogen production from water under visible light. *Nat. Mater.* **2009**, *8*, 76–80. [[CrossRef](#)]
7. Chen, J.; Xiao, X.; Wang, Y.; Ye, Z. Ag nanoparticles decorated WO₃/g-C₃N₄ 2D/2D heterostructure with enhanced photocatalytic activity for organic pollutants degradation. *Appl. Surf. Sci.* **2019**, *467*, 1000–1010. [[CrossRef](#)]
8. Liu, L.; Hu, P.; Cui, W.; Li, X.; Zhang, Z. Increased photocatalytic hydrogen evolution and stability over nano-sheet g-C₃N₄ hybridized CdS core@shell structure. *Int. J. Hydrogen Energy* **2017**, *42*, 17435–17445. [[CrossRef](#)]
9. Wang, Y.; Shi, R.; Lin, J.; Zhu, Y. Enhancement of photocurrent and photocatalytic activity of ZnO hybridized with graphite like C₃N₄. *Energy Environ. Sci.* **2011**, *4*, 2922–2929. [[CrossRef](#)]
10. Han, C.; Gao, Y.; Liu, S.; Ge, L.; Xiao, N.; Dai, D.; Xu, B.; Chen, C. Facile synthesis of AuPd/g-C₃N₄ nanocomposite: An effective strategy to enhance photocatalytic hydrogen evolution activity. *Int. J. Hydrogen Energy* **2017**, *42*, 22765–22775. [[CrossRef](#)]
11. Zang, Y.; Li, L.; Zuo, Y.; Lin, H.; Li, G.; Guan, X. Facile synthesis of composite g-C₃N₄/WO₃: A nontoxic photocatalyst with excellent catalytic activity under visible light. *RSC Adv.* **2013**, *3*, 13646–13650. [[CrossRef](#)]
12. Katsumata, K.; Motoyoshi, R.; Matsushita, N.; Okada, K. Preparation of graphitic carbon nitride (g-C₃N₄)/WO₃ composites and enhanced visible-light-driven photodegradation of acetaldehyde gas. *J. Hazard. Mater.* **2013**, *260*, 475–482. [[CrossRef](#)] [[PubMed](#)]
13. Jin, Z.; Murakami, N.; Tsubota, T.; Ohno, T. Complete oxidation of acetaldehyde over a composite photocatalyst of graphitic carbon nitride and tungsten(VI) oxide under visible-light irradiation. *Appl. Catal. B Environ.* **2014**, *150*, 479–485. [[CrossRef](#)]

14. Zhao, J.L.; Jia, Z.; Shen, X.; Zhou, H.; Ma, L. Facile synthesis of WO₃ nanorods/g-C₃N₄ composites with enhanced photocatalytic activity. *Ceram. Int.* **2015**, *141*, 5600–5606. [[CrossRef](#)]
15. Athanasekou, C.P.; Likodimos, V.; Falaras, P. Recent developments of TiO₂ photocatalysis involving advanced oxidation and reduction reactions in water. *J. Environ. Chem. Eng.* **2018**, *6*, 7386–7394. [[CrossRef](#)]
16. Raptis, D.; Dracopoulos, V.; Lianos, P. Renewable energy production by photoelectrochemical oxidation of organic wastes using WO₃ photoanodes. *J. Hazard. Mater.* **2017**, *333*, 259–264. [[CrossRef](#)]
17. Arfanis, M.K.; Adamou, P.; Moustakas, N.G.; Triantis, T.M.; Kontos, A.G.; Falaras, P. Photocatalytic degradation of salicylic acid and caffeine emerging contaminants using titania nanotubes. *Chem. Eng. J.* **2017**, *130*, 525–536. [[CrossRef](#)]
18. Arfanis, M.K.; Athanasekou, C.P.; Sakellis, E.; Boukos, N.; Ioannidis, N.; Likodimos, V.; Sygellou, L.; Bouroushian, M.; Kontos, A.G.; Falaras, P. Photocatalytic properties of copper—Modified core-shell titania Nanocomposites. *J. Photochem. Photobiol. A* **2019**, *370*, 145–155. [[CrossRef](#)]
19. Ibrahim, I.; Athanasekou, C.; Manolis, G.; Kaltzoglou, A.; Nasikas, N.K.; Katsaros, F.; Devlin, E.; Kontos, A.G.; Falaras, P. Photocatalysis as an advanced reduction process (ARP): The reduction of 4-nitrophenol using titania nanotubes-ferrite nanocomposites. *J. Hazard. Mater.* **2019**, *372*, 37–44. [[CrossRef](#)]
20. Wang, D.; Sun, H.; Luo, Q.; Yang, X.N.; Yin, R. An efficient visible-light photocatalyst prepared from g-C₃N₄ and polyvinyl chloride. *Appl. Catal. B Environ.* **2014**, *156*, 323–330. [[CrossRef](#)]
21. Zhang, Y.; Pan, Q.; Chai, G.; Liang, M.; Dong, G.; Zhang, Q.; Qiu, J. Synthesis and luminescence mechanism of multicolor-emitting g-C₃N₄ nanopowders by low temperature thermal condensation of melamine. *Sci. Rep.* **2013**, *3*, 1943. [[CrossRef](#)]
22. Rajagopal, S.; Nataraj, D.; Mangalaraj, D.; Djaoued, Y.; Robichaud, J.; Khyzhun Yu, O. Controlled Growth of WO₃ Nanostructures with Three Different Morphologies and Their Structural, Optical, and Photodecomposition Studies. *Nanoscale Res. Lett.* **2009**, *4*, 1335–1342. [[CrossRef](#)]
23. Balaji, S.; Djaoued, Y.; Albert, A.S.; Bruning, R.; Beaudoin, N.; Robichaud, J. Porous orthorhombic tungsten oxide thin films: Synthesis, characterization, and application in electrochromic and photochromic devices. *J. Mater. Chem.* **2011**, *21*, 3940–3948. [[CrossRef](#)]
24. Daniel, M.F.; Desbat, B.; Lassegues, J.C. Infrared and Raman Study of WO₃ Tungsten Trioxides and WO₃·xH₂O Tungsten Trioxide Hydrates. *J. Solid State Chem.* **1987**, *67*, 235–247. [[CrossRef](#)]
25. Santato, C.; Odziemkowski, M.K.; Ulmann, M.; Augustynski, J. Crystallographically Oriented Mesoporous WO₃ Films: Synthesis, Characterization, and Applications. *J. Am. Chem. Soc.* **2001**, *123*, 10639–10649. [[CrossRef](#)]
26. Delichere, P.; Falaras, P.; Froment, M.; Hugot-Le Goff, A.; Agius, B. Electrochromism in anodic WO₃ films: Preparation and physicochemical properties of films in the virgin and coloured states. *Thin Solid Films* **1988**, *161*, 35–46. [[CrossRef](#)]
27. Djaoued, Y.; Balaji, S.; Bruning, R. Electrochromic Devices Based on Porous Tungsten Oxide Thin Films. *J. Nanomater.* **2012**, *2012*, 7. [[CrossRef](#)]
28. Xu, C.; Wang, X.; Xu, G.; Chen, Y.; Dai, L. Facile construction of leaf-like WO₃ nanoflakes decorated on g-C₃N₄ towards efficient oxidation of alcohols under mild conditions. *New J. Chem.* **2018**, *42*, 16523–16532. [[CrossRef](#)]
29. Zinin, P.V.; Ming, L.C.; Sharma, S.K.; Khabashesku, V.N.; Liu, X.; Hong, S.; Endo, S.; Acosta, T. Ultraviolet and near-infrared Raman spectroscopy of graphitic C₃N₄ phase. *Chem. Phys. Lett.* **2009**, *472*, 69–73. [[CrossRef](#)]
30. Giannakopoulou, T.; Papailias, I.; Todorova, N.; Boukos, N.; Liu, Y.; Yu, J.; Trapalis, C. Tailoring the energy band gap and edges' potentials of g-C₃N₄/TiO₂ composite photocatalysts for NO_x removal. *Chem. Eng. J.* **2017**, *310*, 571–580. [[CrossRef](#)]
31. Miller, T.S.; Belen Jorge, A.; Suter, T.M.; Sella, A.; Cora, F.; McMillan, P.F. Carbon nitrides: Synthesis and characterization of a new class of functional materials. *Phys. Chem. Chem. Phys.* **2017**, *19*, 15613–15638. [[CrossRef](#)] [[PubMed](#)]
32. Brady, R.L.; Southmayd, D.; Contescu, C.; Zhang, R.; Schwarz, J.A. Surface Area Determination of Supported Oxides: WO₃/Al₂O₃. *J. Catal.* **1991**, *129*, 195–201. [[CrossRef](#)]
33. Moustakas, N.G.; Kontos, A.G.; Likodimos, V.; Katsaros, F.; Boukos, N.; Tsoutsou, D.; Dimoulas, A.; Romanos, G.E.; Dionysiou, D.D.; Falaras, P. Inorganic-organic core-shell titania nanoparticles for efficient visible light activated photocatalysis. *Appl. Catal. B Environ.* **2013**, *130*, 14–24. [[CrossRef](#)]

34. Ibrahim, I.; Kaltzoglou, A.; Athanasekou, C.; Katsaros, F.; Devlin, E.; Kontos, A.G.; Ioannidis, N.; Perraki, M.; Tsakiridis, P.; Sygellou, L.; et al. Magnetically separable TiO₂/CoFe₂O₄/Ag nanocomposites for the photocatalytic reduction of hexavalent chromium pollutant under UV and artificial solar light. *Chem. Eng. J.* **2020**, *381*, 122730. [[CrossRef](#)]
35. Sharma, S.; Basu, S. Highly reusable visible light active hierarchical porous WO₃/SiO₂ monolith in centimeter length scale for enhanced photocatalytic degradation of toxic pollutants. *Sep. Purif. Technol.* **2020**, *231*, 115916. [[CrossRef](#)]
36. Li, S.T.; Wang, P.F.; Wang, R.D.; Liu, Y.F.; Jing, R.S.; Li, Z.; Meng, Z.L.; Liu, Y.Y.; Zhang, Q. One-step co-precipitation method to construct black phosphorus nanosheets/ZnO nanohybrid for enhanced visible light photocatalytic activity. *Appl. Surf. Sci.* **2019**, *497*, 143682. [[CrossRef](#)]



© 2019 by the authors. Licensee MDPI, Basel, Switzerland. This article is an open access article distributed under the terms and conditions of the Creative Commons Attribution (CC BY) license (<http://creativecommons.org/licenses/by/4.0/>).